

## Measurement and Prediction of Stresses during Casting of a Steel Bar

D. Galles<sup>1</sup>, C. Monroe<sup>2</sup>, and C. Beckermann<sup>1</sup>

<sup>1</sup>Dept. Mechanical and Industrial Engineering, University of Iowa, Iowa City, Iowa 52242

<sup>2</sup>Champaign Simulation Center, Caterpillar, Inc., Champaign, Illinois, 61820

### Abstract

Stresses and displacements are predicted in a steel casting from pouring temperature down to room temperature using a viscoplastic stress model that considers damage. Temperature, force, and displacement data are acquired by performing *in situ* casting experiments of a one-inch square cross-section bar, 12 inches long. Two experiments are performed: (1) a strained casting and (2) an unrestrained casting. The strained casting is placed in a restraint, and a turnbuckle is used to induce stresses in the casting at high temperatures. The unrestrained casting is allowed to contract freely with no restraints. Thermal simulations are performed with MAGMAsoft<sup>1</sup> simulation software to solve for the evolution of the thermal field. Viscoplastic equation parameters are estimated from data found in the literature. Using the simulated thermal results and measured forces as boundary conditions, the displacement of the bar is predicted using the commercial finite element software package ABAQUS<sup>2</sup> with a user-defined UMAT subroutine. The results show reasonable agreement between predicted and measured displacement.

### 1. Introduction

Dimensional differences between the mold cavity and the casting are of great concern to all steel foundries. When no restraints due to cores and the mold are present, the casting is said to contract freely. For such free thermal contraction of steel, final casting dimensions are straightforward to predict and amount to a pattern allowance of approximately 2.3%. However, mechanical interactions between the casting and the mold and cores generate stresses within the casting and may result in gross distortions. For complex shaped castings, non-uniform cooling also creates strains that result in permanent distortions. During solidification, such strain can lead to hot tears<sup>3</sup>. At lower temperatures, cold cracks can occur. Casting simulation is traditionally used to predict temperatures during casting and the presence of porosity. More recently, mechanical models have been coupled to casting simulation in order to predict distortions, hot tears and cracks, and residual stresses. However, these stress models are only at the beginning of

their development and have not yet been proven to predict distortions and final casting dimensions accurately. In this respect, it is crucial that realistic constitutive models are used that describe the mechanical behavior of both the mold and the steel. Such models require knowledge of the mechanical properties over the entire range of temperatures and strain rates encountered during casting. The focus in this study is to predict stresses and displacements in a steel casting and validate those predictions with measured data acquired from *in situ* casting experiments.

Because the microstructure created during solidification differs from reheated samples, obtaining experimental data through *in situ* testing is preferable. However, due to the difficulty of measuring displacement in steel at high temperatures, studies in which *in situ* testing is used in conjunction with computational deformation models are limited. Monroe and Beckermann<sup>4</sup> performed *in situ* experiments of a steel bar to predict hot tearing. Rowan *et al.*<sup>5</sup> performed the submerged split chill contraction (SSCC) experiment to predict forces in a solidifying steel shell.

In this study, a viscoplastic constitutive model that considers damage is used to predict stresses and displacements in a steel casting. Temperature, force, and displacement data are acquired from *in situ* strained casting experiments, in which a tensile force is applied to a simple bar casting at high temperatures. An additional unrestrained experiment is also performed in which no force is applied, and the casting is allowed to contract freely. Thermal simulations are then performed to determine the evolution of the thermal field throughout the casting. The temperature-dependent mechanical properties in the viscoplastic constitutive relation are estimated using data from the literature. The thermal fields and mechanical properties are then supplied to a user-defined UMAT subroutine in the finite element code ABAQUS. An initial simulation is performed to predict the displacements in the unrestrained casting. Finally, the strained casting experiment is simulated to predict the measured displacements using the measured applied force as input.

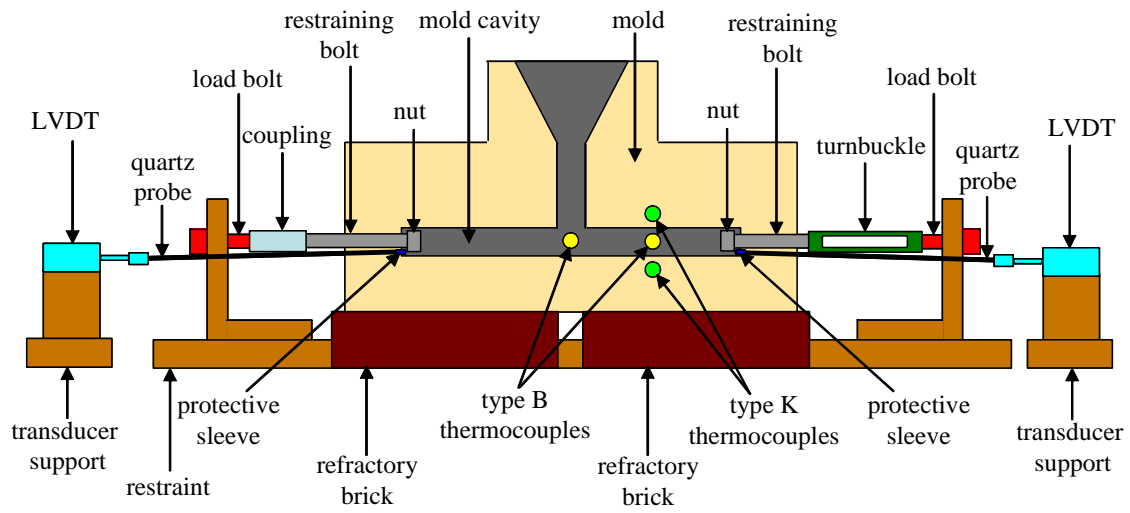
## **2. Description of Experiments**

### 2.1 Experimental Setup

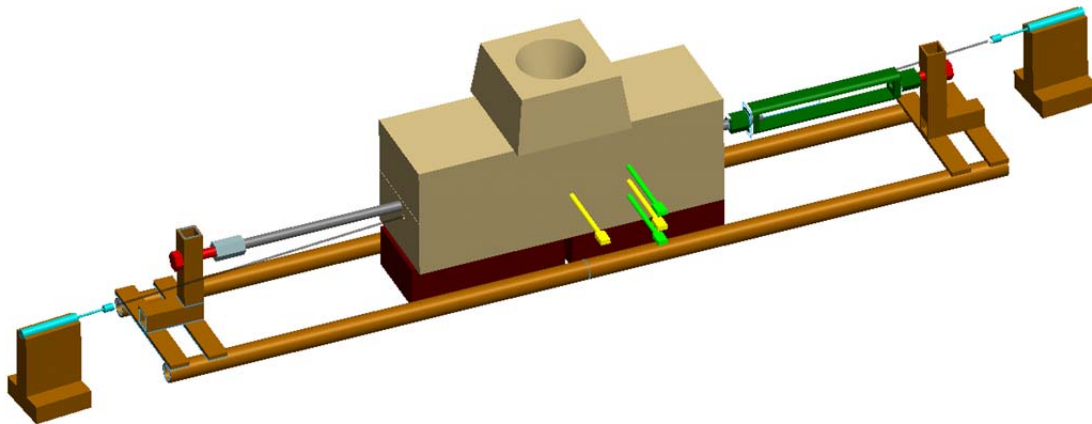
Experimental data was acquired by performing casting experiments at the University of Northern Iowa's Metal Casting Center. The castings were poured from a 200 lb heat and prepared in an induction furnace. The target chemistry was WCB steel and compositions from each experiment are shown in Table 1. The molds were made using silicon sand bonded with a phenolic urethane binder. Schematic and Pro-E drawings of the strained bar experimental setup

are shown in Fig. 1. Removal of the restraint, load bolts, restraining bolts, nuts, coupling, and turnbuckle in Fig. 1 reduces the strained bar to the unrestrained bar.

To acquire temperature, force, and displacement data, a variety of measurement devices were used. Temperatures in the casting and mold were measured using type B and type K thermocouples, respectively. The type B thermocouples were encased in quartz tubing to protect them from the molten steel. Placement of the thermocouples and mold dimensions are shown in Fig. 2. Force data was acquired with an Omega LCS-1/2-2L load bolt on each side of the restraint. Restraining bolts were constructed from half-inch threaded steel rod and cut to appropriate lengths. Nuts were threaded onto the ends of the restraining bolts inside the mold cavity to ensure the restraining bolts were firmly anchored in the casting and would not slip when the induced straining occurred. A coupling connected the restraining bolt to the load bolt on the left side of the schematic in Fig. 1, and a turnbuckle connected the restraining bolt to the load bolt on the right side. Care was taken to assure the load bolts, restraining bolts, and casting were inline with each other. Once poured, the casting was allowed to solidify until it was coherent and could transmit stresses, at which time the turnbuckle was engaged to induce strain in the bar. This “time to coherency” was determined through a trial-and-error method in which strains were induced earlier in each successive experiment until the casting failed. The goal was to induce strain before the bar had fully solidified. Displacement measurements were taken with an Omega LD620-5 LVDT (linear variable differential transformer) at each end of the mold. A 3 mm diameter quartz rod was connected at one end to the LVDT, and the other end was inserted 3-5 mm into the mold cavity. To ensure the quartz rod did not slip in the casting, the end of the rod was bulged into a spherical shape using an oxy-acetylene torch. Quartz is a suitable material to use in this application because of its high melting point and low thermal expansion. However, it is also extremely brittle. The quartz rods frequently broke during the experiments due to the build-up of compressive stresses as the casting cooled. To alleviate this problem, protective metal sleeves were inserted over the bulged ends inside the mold cavity. The total length change in the bar was calculated by adding the displacements of the two LVDT’s. Note from Fig. 1 that the supports holding the LVDT’s were on the ground.



(a) Schematic



(b) Pro-E drawing

Figure 1. Experimental setup of strained bar.

Table 1. Casting chemistries of unrestrained and strained experiments.

Experiment	Casting Chemistry										
	%C	%Si	%Mn	%P	%S	%Cr	%Mo	%Ni	%Al	%Cu	%Fe
Unrestrained 1	0.21	.050	0.52	0.072	0.002	0.08	0.01	0.02	0.070	0.08	98.38
Unrestrained 2	0.32	0.69	0.64	0.025	0.014	0.23	0.02	0.09	0.054	0.10	97.71
Unrestrained 3	0.25	0.59	0.55	0.012	0.014	0.04	0.00	0.01	0.069	0.04	98.40
Strained 1	0.25	0.58	0.62	0.022	0.016	0.03	0.02	0.02	0.087	0.05	98.29
Strained 2	0.25	0.61	0.56	0.021	0.017	0.10	0.01	0.04	0.071	0.08	98.18
Strained 3	0.25	0.45	0.46	0.019	0.017	0.04	0.00	0.01	0.045	0.03	98.67
Strained 4	0.20	0.41	0.42	0.015	0.009	0.01	0.01	0.01	0.028	0.04	98.83
Strained 5	0.41	2.76	0.39	0.089	0.031	0.01	0.00	0.04	0.035	0.75	95.04

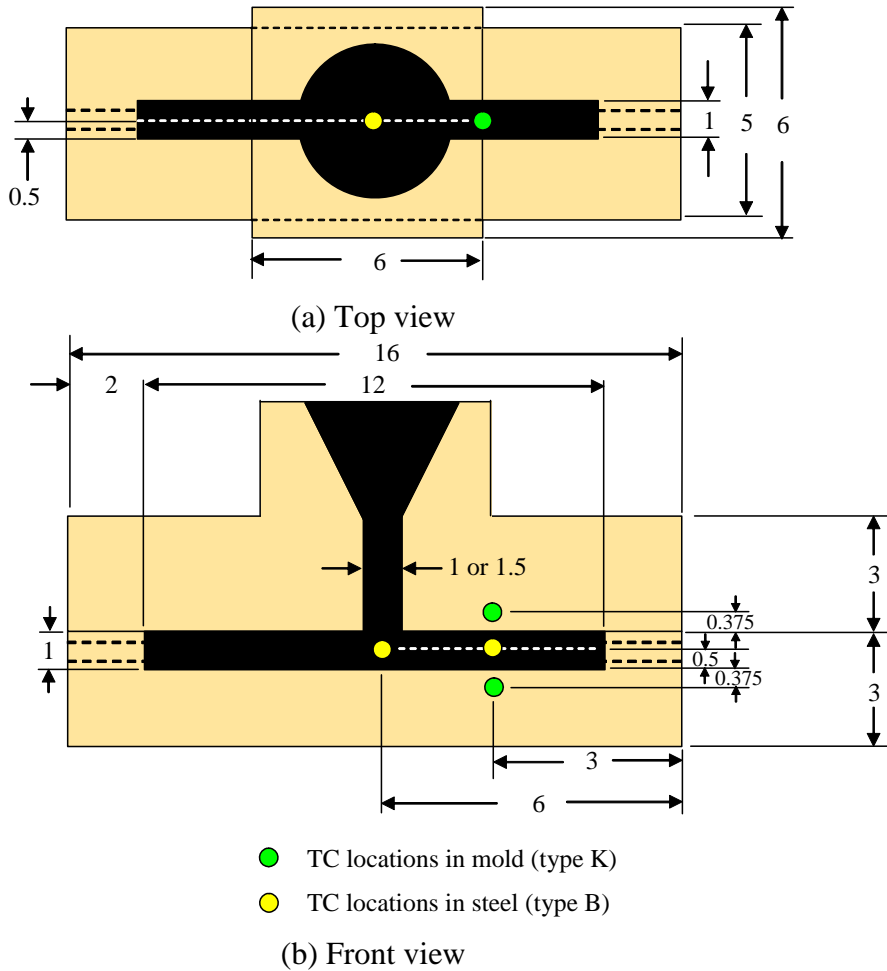


Figure 2. Mold geometry of unrestrained and strained bar experiments with thermocouple locations.

Experimental data was collected using an IOtech model 3005 Personal DAQ system connected to a laptop computer. DASyLab software was used to acquire the data from the 3005 Personal DAQ. A sampling rate of 2 Hz was used at high temperatures and switched to 0.5 Hz at lower temperatures (< 800 °C).

## 2.2 Experimental Results

Final castings of the unrestrained and strained bars are shown in Fig. 3. Table 2 shows additional experimental details, including the color code of the curves used on the plots of the experimental results, the size of the sprue for the experiment, and the liquidus temperature that is predicted by IDS<sup>6</sup> software package. Initial experiments were performed using a 1-inch diameter sprue. However, it was suspected that porosity formation was occurring under the sprue. Therefore, the Strained 4 and Strained 5 experiments were performed with a 1.5-inch diameter sprue. Figs. 4(a) and 4(b) show radiographs of the 1-inch sprue and 1.5-inch sprue strained bars, respectively. Close examination of the radiographs reveal the formation of cracks along the length of the bar. These cracks are a result of tensile stresses in the bars at high temperatures.









Fig. 5 shows the thermal results in the casting for all experiments.  $T_{sprue}$  and  $T_{right}$  refer the measured temperatures of the thermocouples located directly under and to the right of the sprue, respectively, as shown in Fig. 2. The thermal results are very reproducible. Due to the increased sprue size, Strained 4 and Strained 5 cool at a slower rate than the castings with a smaller sprue. The solid-state transformation occurs at similar temperatures for all experiments at approximately 675 °C. The liquidus temperature was not measured due to: (1) the superheat was not large enough, (2) the thermocouples have a delayed response time, and (3) the casting was small.

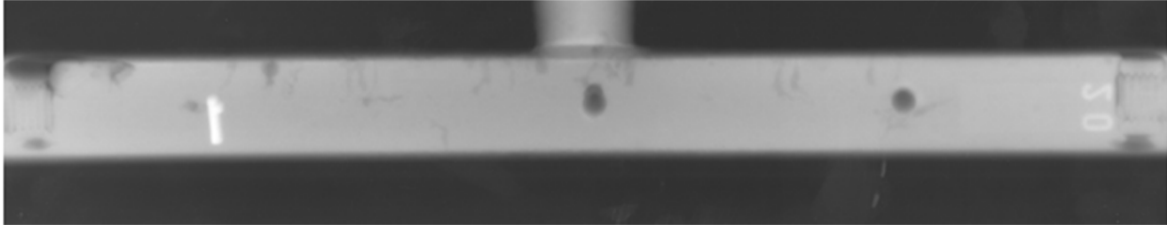
Displacement results are shown in Fig. 6. The unrestrained experiments show excellent reproducibility. Slight differences are seen at the solid-state transformation at approximately 800 seconds. The displacements for the strained bar experiments vary depending on when the induced straining began and how long it lasted. Fig. 6(c) shows the periods of induced straining for each strained bar experiment.



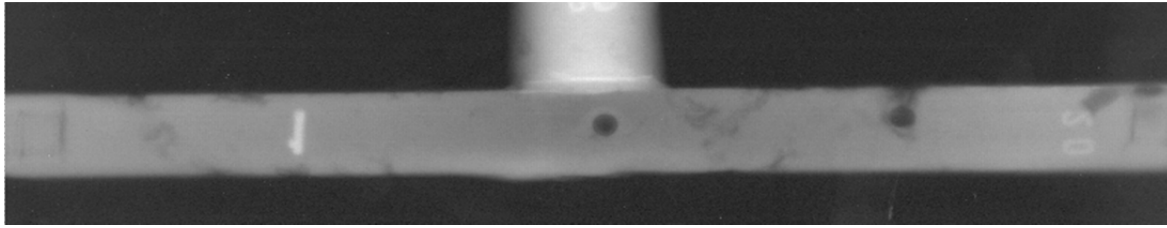
Figure 3. Final unrestrained and strained castings.

Table 2. Additional experimental details

Experiment	Additional Experimental Details		
	Color of Curve on Experimental Plots	Sprue Size	IDS Liquidus (°C)
Unrestrained 1		1 inch	1511
Unrestrained 2		1 inch	1499
Unrestrained 3		1 inch	1508
Strained 1		1 inch	1507
Strained 2		1 inch	1507
Strained 3		1 inch	1499
Strained 4		1.5 inches	1515
Strained 5		1.5 inches	1485



(a) 1-inch sprue



(b) 1.5-inch sprue

Figure 4. Radiographs of strained bar castings

A comparison of the force and displacement results from the Strained 5 experiment is shown in Fig. 7. The measured turnbuckle data are obtained from the instrumentation located on the side of the mold containing the turnbuckle, as shown in Fig. 2. The measured non-turnbuckle data are obtained from the opposite side. Fig. 7(c) shows that as the turnbuckle was turning, the force measurements are in good agreement. However, when the turnbuckle stops, the turnbuckle force relaxes. This is due to an interaction between the sprue and mold, unfortunately. One of the goals of the present study was to eliminate interaction between the mold and the casting. The mold was designed so forces in the casting were transmitted only through the restraining bolts in a controlled manner. This was not the case, however, and the difference in the displacement results in Fig. 7 confirms that the difference in forces is real, i.e., not an error in the load bolt measurements. Additionally, the load bolts were calibrated before and after the experiment. This difference in forces was seen in all strained bar experiments. This discrepancy requires further attention and will be discussed in the conclusion. All non-turnbuckle force measurements are shown in Fig. 8. Nominal stresses were derived by dividing the non-turnbuckle force by the cross-sectional area of the casting.

By differentiating the measured temperatures (shown in Fig. 5) with respect to time, temperature dependent cooling rates were calculated and are shown in Fig. 9. To smooth the cooling curves, a 21-point running average is used. At the onset of solidification, latent heat is

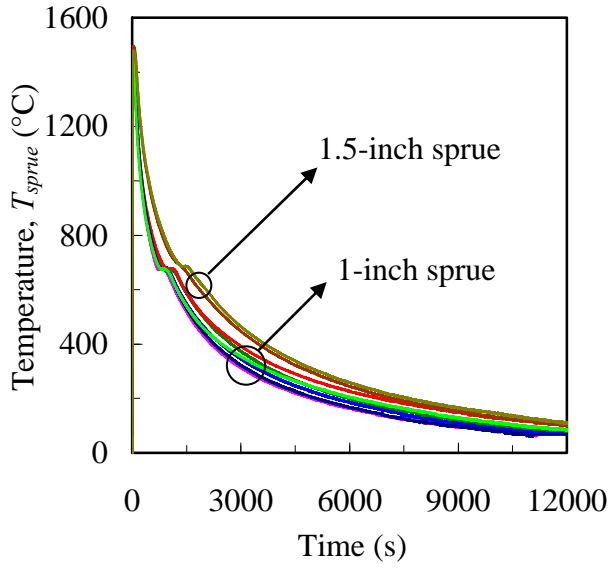


released and the cooling rate decreases to zero. Throughout the solidification range, the amount of latent heat released decreases with decreasing temperature. Consequently, the cooling rate increases. As a result, the maximum cooling rate is observed at the solidus temperature. The solidus values for all thermal results are shown in table 3.

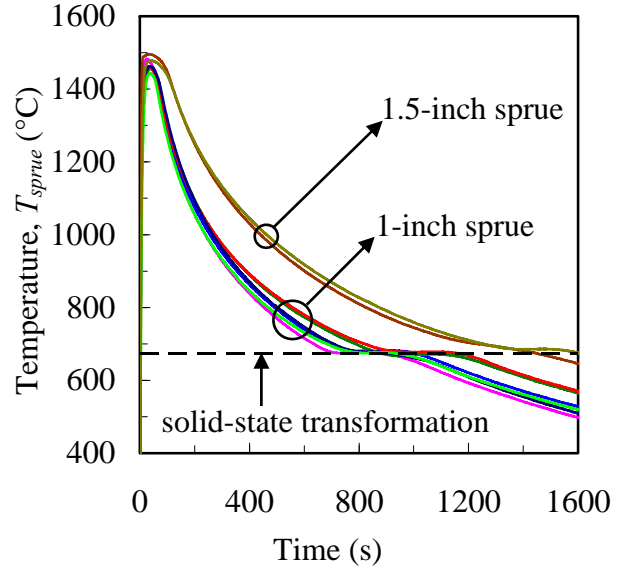
The total strain of the bar can be written as

$$\varepsilon_{total} = \varepsilon_{mechanical} + \varepsilon_{thermal} \quad (1)$$

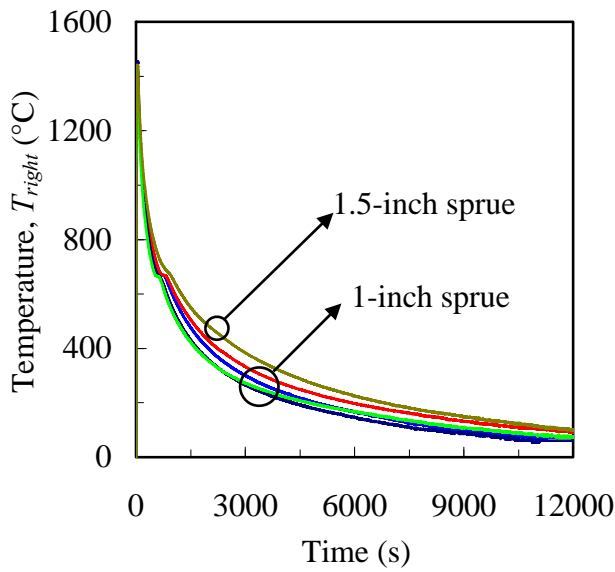
where  $\varepsilon_{total}$  is the total strain,  $\varepsilon_{mechanical}$  is the mechanical strain, and  $\varepsilon_{thermal}$  is the thermal strain. Subtracting the unrestrained displacement from the strained displacement will not give the correct mechanical strain because the restraining bolts have a chilling effect on the strained bar and cool the casting at a different rate than the unrestrained bar near the ends of the bars. Therefore, to calculate the mechanical strain, an ABAQUS simulation was performed on the strained bar casting with a zero-force boundary condition to calculate the thermal strain in the strained bar. The assumption that the simulated thermal strain is a good approximation of the actual thermal strain will be validated in the results section. The calculated thermal strain was then subtracted from the total measured strain of the bar to give the mechanical strain. A plot of the nominal stress-mechanical strain from the Strained 1 experiment is shown in Fig. 10. Temperatures at the sprue location and strain rates are listed at different strains. Since this plot is temperature dependent, it is not to be confused with an isothermal stress-strain plot. The initial increase in stress appears to be a linear function of strain. However, this is not the elastic region. Stresses initially increase because the bar is not yet fully solid, and the cross-sectional area is increasing as the liquid steel solidifies. Plastic deformation is certainly occurring in this region. After the bar is fully solidified, the stress remains relatively constant until the solid-state transformation. Strain rates are on the order of  $10^{-5}$  /s before the solid-state transformation and two orders of magnitude lower after the transformation.



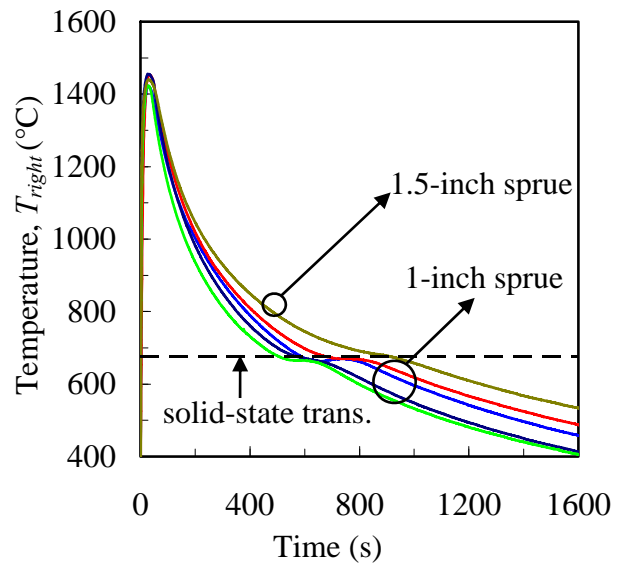
(a) Large time scale at sprue location.



(b) Medium time scale at sprue location.

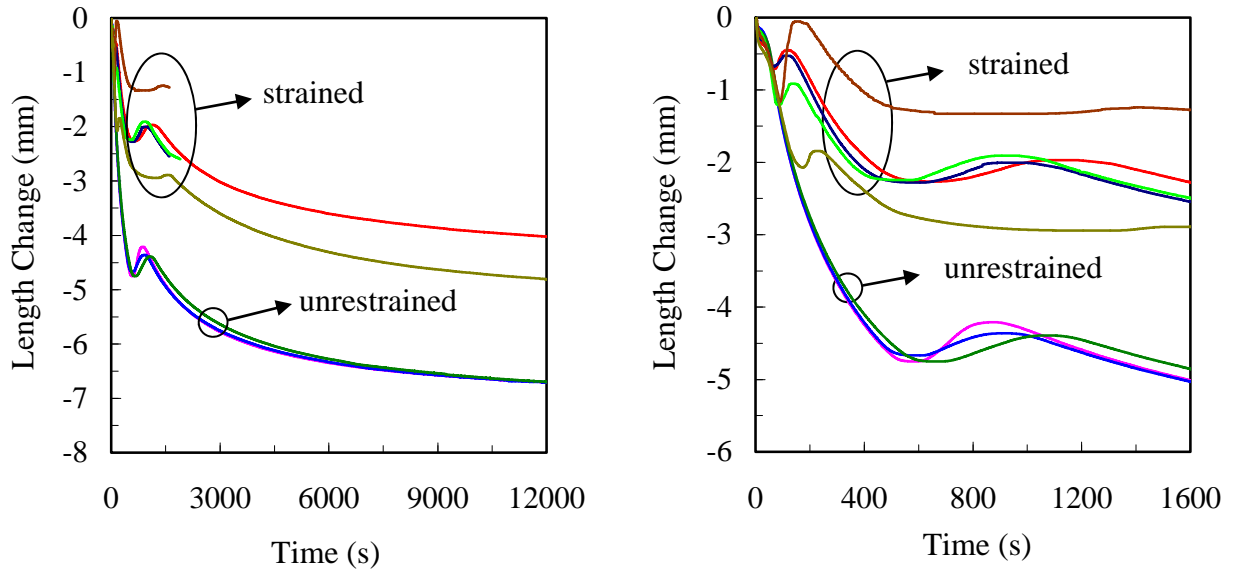


(c) Large time scale at right location.



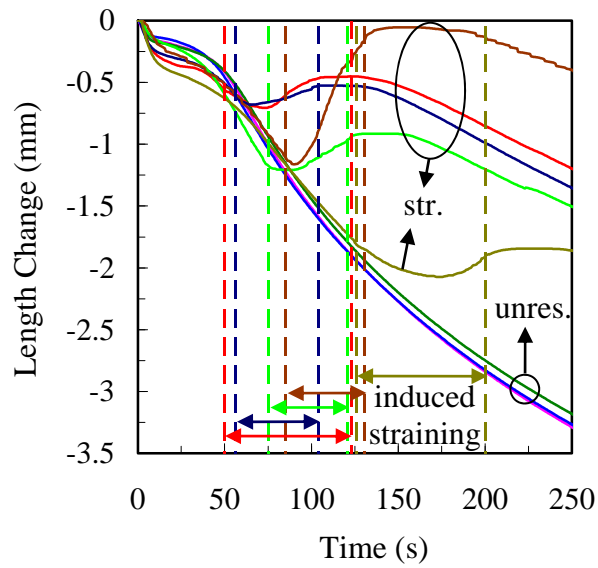
(d) Medium time scale at right location.

Figure 5. Thermal results in the casting for all unrestrained and strained experiments.  $T_{sprue}$  and  $T_{right}$  refer the measured temperatures of the thermocouples located directly under and to the right of the sprue, respectively, as shown in Fig. 2.



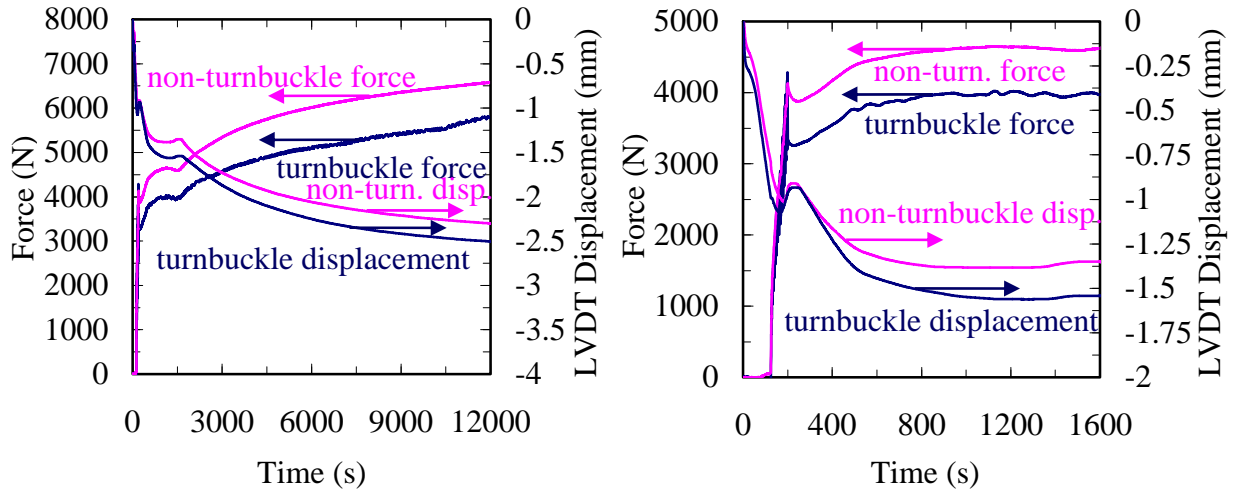
(a) Large time scale

(b) Medium time scale



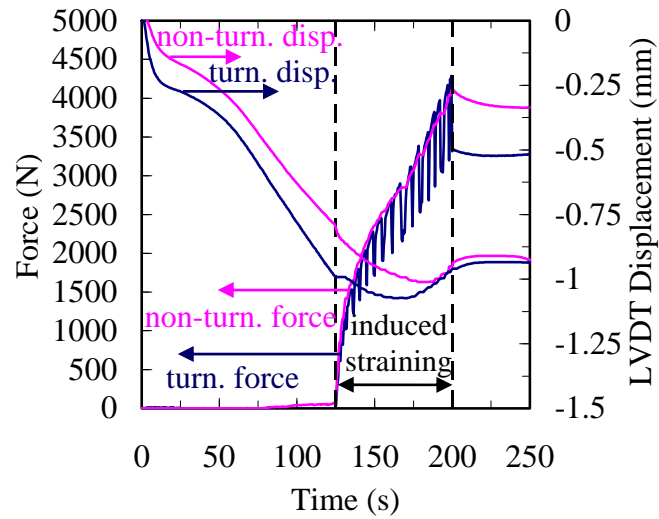
(c) Small time scale showing induced straining periods

Figure 6. Length change in the bar (calculated by adding the values of the LVDT measurements together).



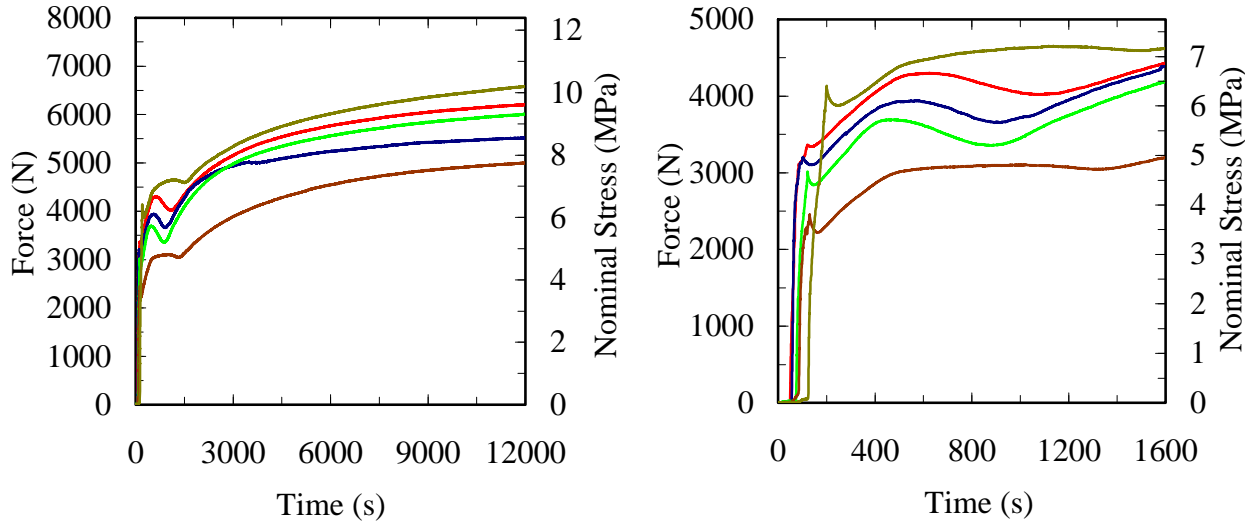
(a) Large time scale

(b) Medium time scale



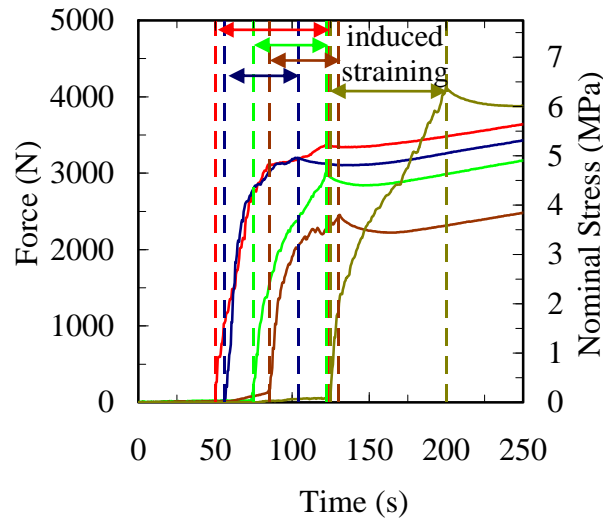
(c) Small time scale showing the induced straining region.

Figure 7. A comparison of the turnbuckle and non-turnbuckle measured forces and LVDT displacements from the Strained 5 experiment. The measured turnbuckle data are obtained from the instrumentation located on the side of the mold containing the turnbuckle, as shown in Fig. 2. The measured non-turnbuckle data are obtained from the opposite side.



(a) Large time scale

(b) Medium time scale



(c) Small time scale showing induced straining periods

Figure 8. Non-turnbuckle force results. The measured non-turnbuckle forces are obtained from the load bolt located on the side of the mold opposite of the turnbuckle, as shown in Fig. 2. The nominal stress is calculated by dividing the non-turnbuckle forces by the cross-sectional area of the bar.

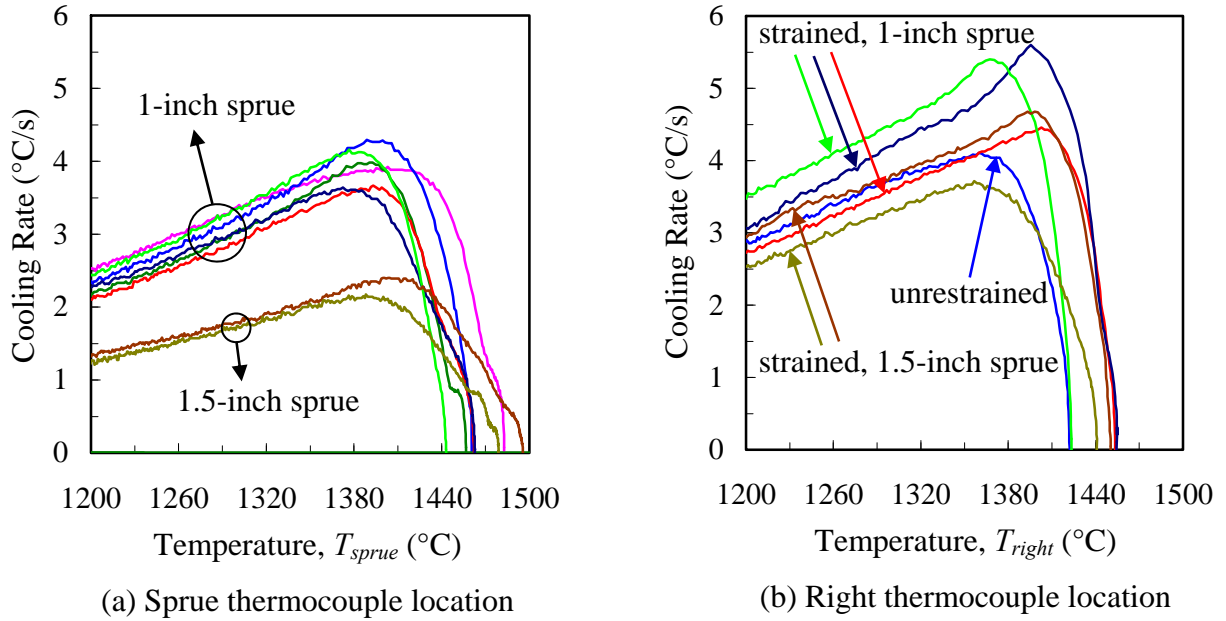


Figure 9. Cooling rates, which were calculated from the thermal results in Fig. 5.  $T_{sprue}$  and  $T_{right}$  refer the measured temperatures of the thermocouples located directly under and to the right of the sprue, respectively, as shown in Fig. 2.

Table 3. Solidus temperatures, which are the temperatures at the maximum measured cooling rates from Fig. 9.

Experiment	Measured Solidus	
	Sprue location (°C)	Right location (°C)
Unrestrained 1	1410	N/A
Unrestrained 2	1405	1375
Unrestrained 3	1392	N/A
Strained 1	1405	1417
Strained 2	1387	1413
Strained 3	1393	1385
Strained 4	1415	1408
Strained 5	1400	1370

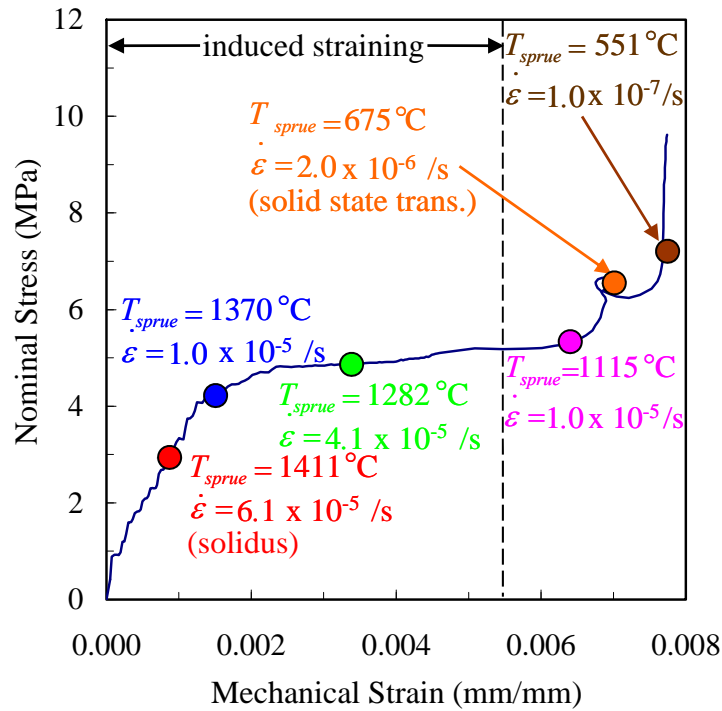
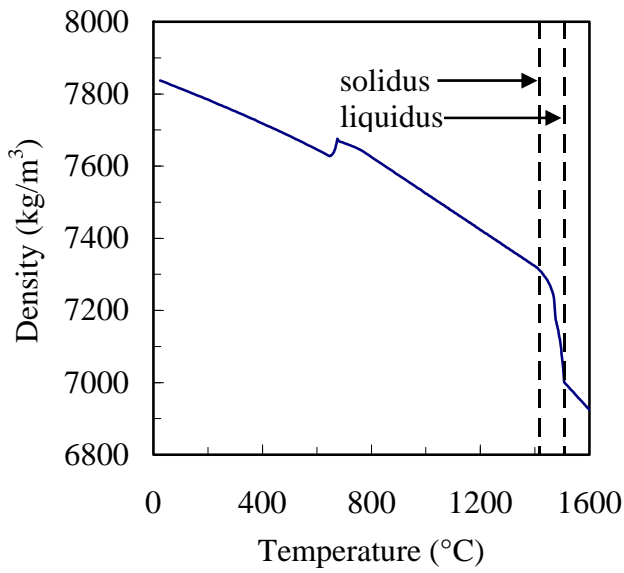


Figure 10. Nominal stress/mechanical strain curve from Strained 1 experiment. The nominal stress was calculated by dividing the force by the cross-sectional area of the bar. Mechanical strain was calculated by subtracting the simulated thermal axial strain from the total measured axial strain in the bar. Strain rates at various temperatures are also shown along with the induced straining period.

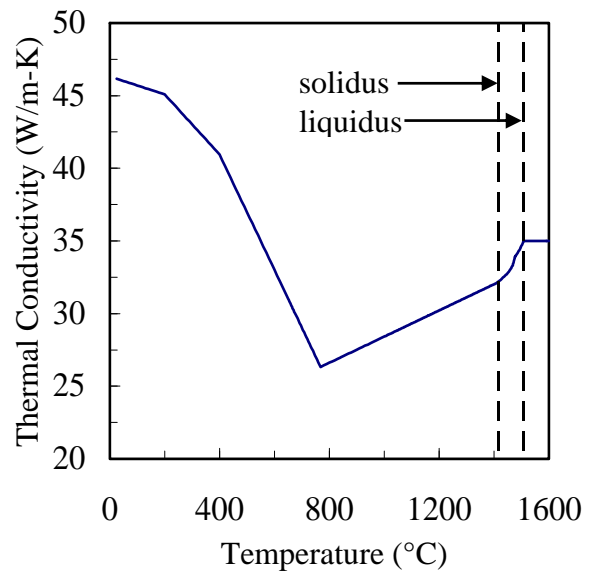
### 3. Thermophysical Properties and Thermal Simulations

#### 3.1 Thermophysical Properties

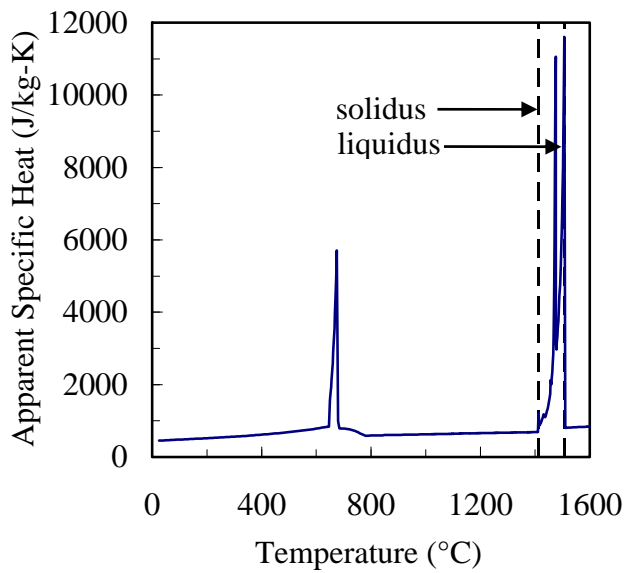
The temperature dependent thermophysical properties and solid phase fraction for the steel were generated in IDS using the chemistry of the Strained 1 experiment. These properties, which include density, thermal conductivity, and apparent specific heat, are shown in Fig. 11. The apparent specific heat, shown in Fig. 11(c), takes into account the latent heat that is released during solidification and phase changes. Sharp changes in figures 11(a) through 11(c) at approximately 700 °C are due to the solid-state transformation. Additionally, IDS predicted liquidus, solidus, and latent heat of solidification values of 1507 °C, 1416 °C, and 253.0 kJ/kg, respectively. Properties were also generated for the Unrestrained 2 experiment and had similar temperature-dependent values as those in Fig. 11. Predicted liquidus, solidus, and latent heat values for Unrestrained 2 were 1499 °C, 1390 °C, and 249.3 kJ/kg, respectively.



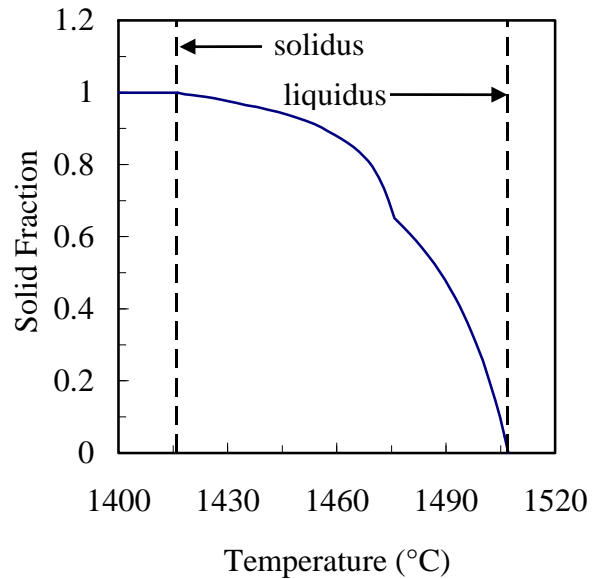
(a) Density



(b) Thermal conductivity



(c) Apparent specific heat



(d) Solid fraction

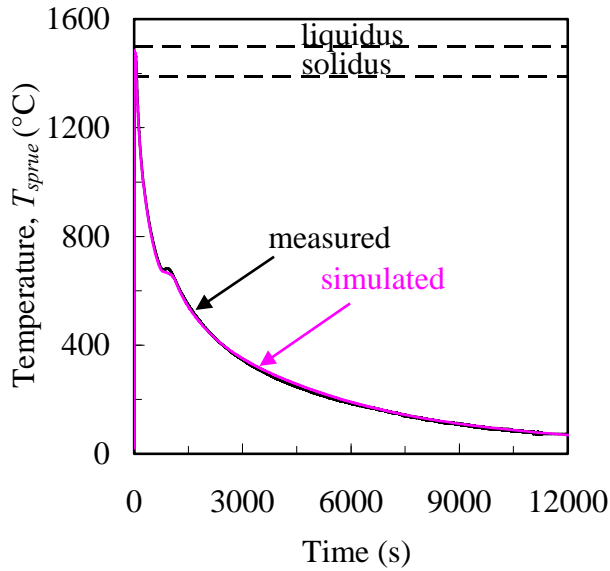
Figure 11. Thermophysical temperature-dependent properties and solid phase fraction were generated in IDS using the casting chemistry of the Strained 1 experiment.



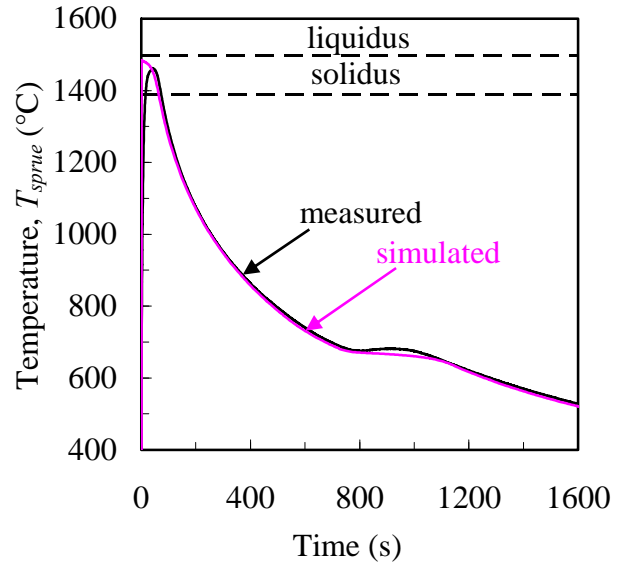
### 3.2 Thermal Simulations

Thermal simulations were performed in MAGMAsoft. Virtual thermocouples were placed in the model at the locations of the type B thermocouples shown in Fig. 2. The cast alloy was modeled using the strained and unrestrained datasets generated in section 3.1. To model the mold and restraining bolts, Furan and Steel were used from the MAGMAsoft database, respectively. Filling and solidification were calculated for the simulations. For the initial simulation, a 10 °C superheat was used for the pouring temperature, and a constant value of 1000 W/m<sup>2</sup>-K was used for the interfacial heat transfer coefficient.

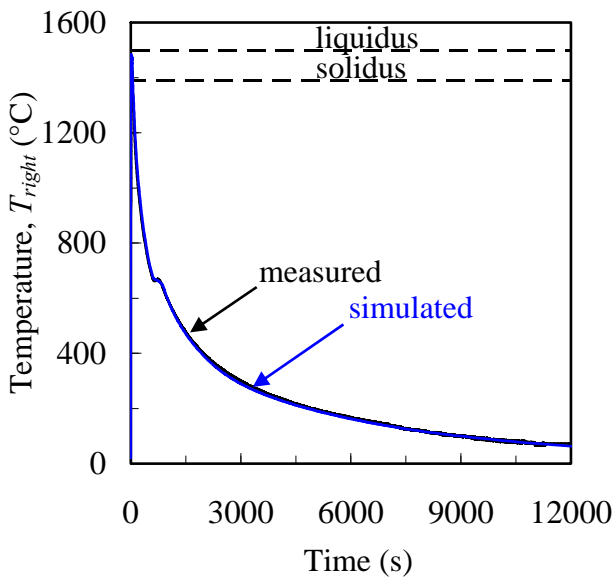
Results of the thermal simulations are shown for the unrestrained and restrained bars in Figs. 12 and 13, respectively. Through a trial-and-error method, the predicted and measured temperature curves were matched by adjusting the pouring temperature and/or interfacial heat transfer coefficient. By adjusting the pouring temperature, time to the solidus temperature was matched. Pouring temperatures for the strained and unrestrained cases were adjusted to 1500 °C and 1485 °C, respectively. Good agreement was seen only after decreasing the pouring temperatures to values below the liquidus temperatures. At temperatures below the solidus, the curves were matched by decreasing the interfacial heat transfer coefficient. This decrease is realistic and reflects the formation of an air gap between the casting and the mold during cooling. To match the strained case, the interfacial heat transfer coefficient was sharply decreased under 1000 °C, as shown in Fig. 14. However, the unrestrained case showed the best agreement when using a constant value of 1000 W/m<sup>2</sup>-K. While it is expected that the interfacial heat transfer coefficient should be the same for both experiments, the focus of the current study is to predict stresses and displacements. Thermal strain predicted by the model depends on the predicted temperature results, since deformation is driven by density changes during solidification and cooling. Additionally, predictions of the plastic strain by the viscoplastic constitutive model require accurate temperature-dependent mechanical properties. Therefore, it is essential to match the predicted and measured results as closely as possible. For this reason, two different heat transfer coefficients were used. Simulated thermal fields were then generated at multiple time steps. These results were then transferred from the MAGMAsoft mesh to the ABAQUS mesh.



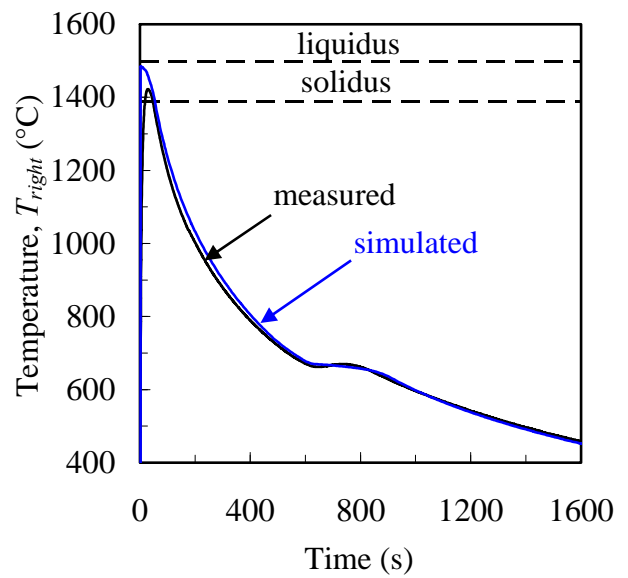
(a) Large time scale at sprue location



(b) Medium time scale at sprue location

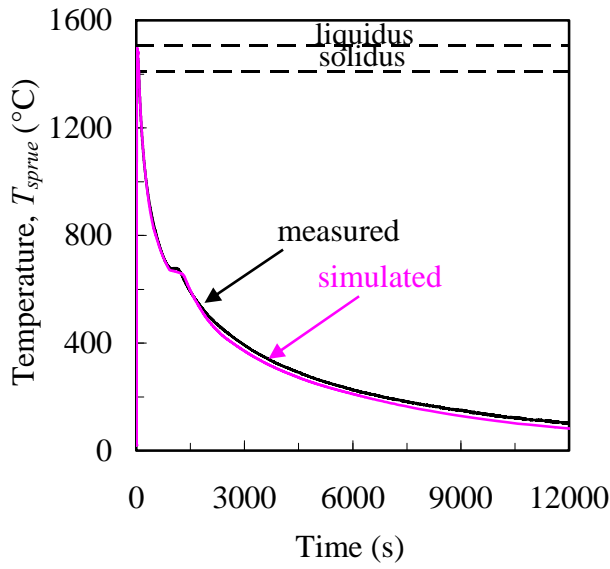


(c) Large time scale at right location

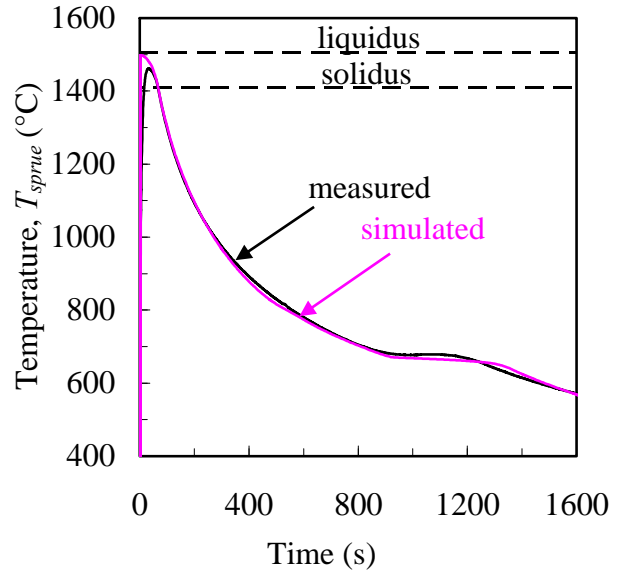


(d) Medium time scale at right location

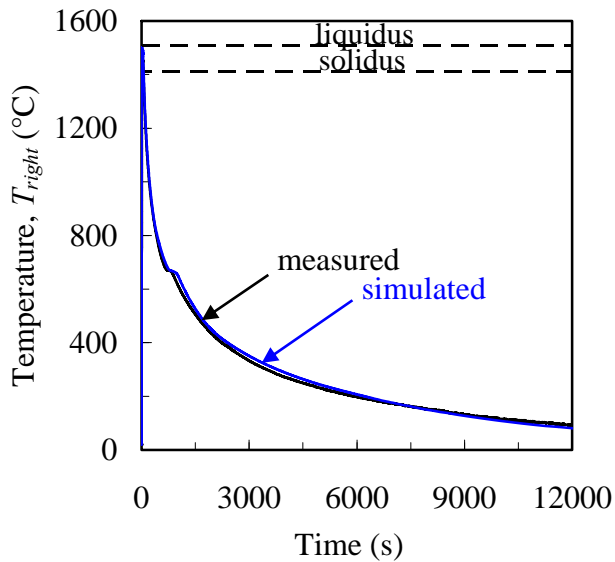
Figure 12. Thermal simulations of unrestrained bar. The initial pouring temperature was adjusted to get agreement between measured and simulated data.  $T_{sprue}$  and  $T_{right}$  refer the measured temperatures of the thermocouples located directly under and to the right of the sprue, respectively, as shown in Fig. 2.



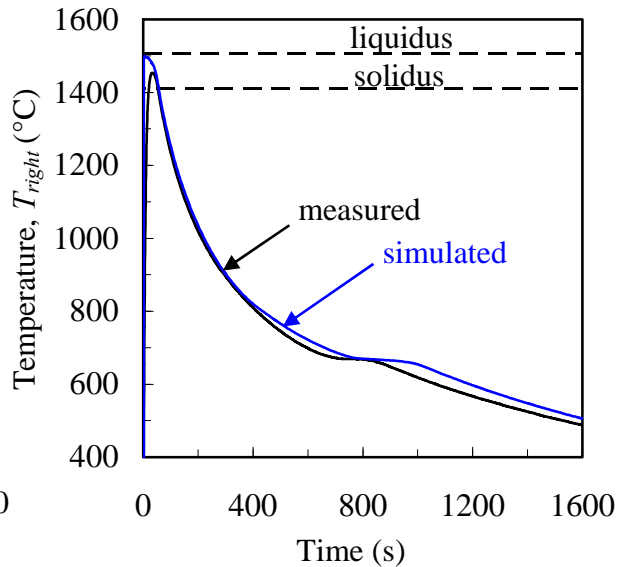
(a) Large time scale at sprue location



(b) Medium time scale at sprue location



(c) Large time scale at right location



(d) Medium time scale at right location

Figure 13. Thermal simulations of the strained bar. Pouring temperature and interfacial heat transfer coefficient were adjusted to obtain good agreement between measured and simulated data.  $T_{sprue}$  and  $T_{right}$  refer the measured temperatures of the thermocouples located directly under and to the right of the sprue, respectively, as shown in Fig. 2.

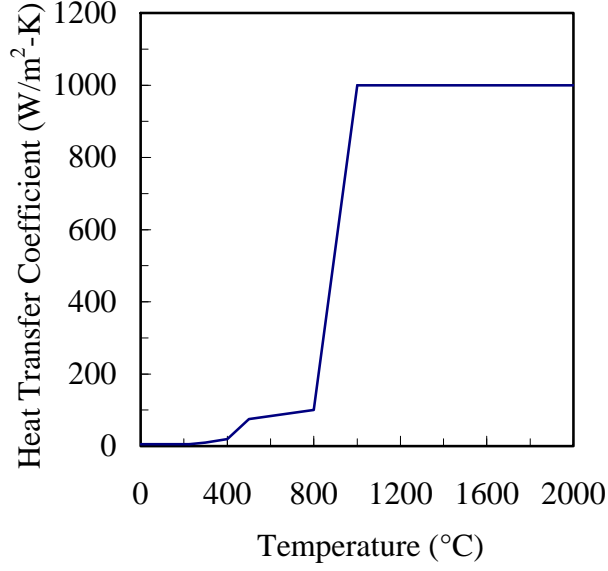


Figure 14. Temperature-dependent interfacial heat transfer coefficient used for thermal simulation of Strained 1 experiment.

#### 4. Stress Model

To model solid deformation, the solid momentum equation must be solved for and is given by

$$\nabla \cdot \boldsymbol{\sigma} = 0 \quad (2)$$

where  $\boldsymbol{\sigma}$  is the stress tensor.

Assuming small strain theory, the total strain,  $\boldsymbol{\varepsilon}$ , can be decomposed into the elastic ( $e$ ), thermal ( $th$ ), and viscoplastic ( $vp$ ) components as

$$\boldsymbol{\varepsilon} = \boldsymbol{\varepsilon}_e + \boldsymbol{\varepsilon}_{th} + \boldsymbol{\varepsilon}_{vp} \quad (3)$$

Using Hooke's law, the elastic strain is determined by

$$\boldsymbol{\sigma} = \mathbf{C}_e : \boldsymbol{\varepsilon}_e \quad (4)$$

where  $\mathbf{C}_e$  is the elastic stiffness tensor. Assuming a homogeneous and isotropic material,  $\mathbf{C}_e$  is given by

$$\mathbf{C}_e = \frac{E}{3(1-2\nu)} \mathbf{I} \otimes \mathbf{I} + \frac{E}{(1+\nu)} \mathbf{I}_{dev} \quad (5)$$

where  $E$  is Young's modulus,  $\nu$  is Poisson's ratio,  $\mathbf{I}$  is the fourth-order identity tensor, and  $\mathbf{I}_{dev}$  is the fourth-order deviatoric identity tensor.

The thermal strain is given by

$$\boldsymbol{\varepsilon}_{th} = \alpha(T - T_{coh}) \mathbf{I} \quad (6)$$

where  $T_{coh}$  is the temperature at which the material reaches coherency and begins to thermally contract. For the present study,  $T_{coh}$  is taken as the 100% solidus temperature. Additionally,  $\mathbf{I}$  is the second-order identity tensor, and  $\alpha$  is the coefficient of total thermal expansion defined as

$$\alpha = \frac{1}{(T - T_{coh})} \int_{T_{coh}}^T -\frac{1}{3\rho_s} \frac{d\rho_s}{dT} dT \quad (7)$$

where  $\rho_s$  is the solid density. Equation (7) is the form of the coefficient of thermal expansion that is required by ABAQUS. The temperature dependence of  $\alpha$  is shown in Fig. 15.

The viscoplastic strain is determined from the flow condition. The flow condition limits the maximum stress the material can hold by keeping the equivalent stress less than or equal to the yield stress. When the equivalent stress exceeds the yield stress, the plastic strain is increased to satisfy  $\sigma_{eq} \leq \sigma_{dy}$ . The equivalent stress is given by

$$\sigma_{eq}^2 = A_1(g_s)q^2 + A_2(g_s)p^2 \quad (8)$$

where  $q$  is the von Mises stress and  $p$  is the pressure. The functions  $A_1$  and  $A_2$  are from the Cocks model and depend on the solid fraction<sup>7</sup>. In the limit where the solid fraction is unity, equation (8) reduces to the von Mises solution, where  $A_1$  is equal to unity and  $A_2$  is equal to zero.

The yield stress for the solid material is given by

$$\sigma_{dy} = \sigma_0 \left( 1 + \frac{\varepsilon_{eq}}{\varepsilon_0} \right)^n \left( 1 + \frac{\dot{\varepsilon}_{eq}}{\dot{\varepsilon}_0} \right)^m \quad (9)$$

where  $\sigma_0$  is the initial yield stress,  $\varepsilon_{eq}$  is the equivalent plastic strain,  $\varepsilon_0$  is the reference shear strain and given by  $\varepsilon_0 = \sigma_0 n / E$ ,  $\dot{\varepsilon}_{eq}$  is the equivalent plastic strain rate,  $\dot{\varepsilon}_0$  is the reference strain rate,  $n$  is the strain hardening exponent,  $m$  is the strain rate sensitivity exponent, and  $E$  is Young's modulus.

Damage due to solid deformation is porosity created by volumetric plastic strain. The volume fraction damage (porosity) is found by integrating over time the volumetric part of the viscoplastic strain rate as

$$g_p = \int_{t_{cr}}^t g_s \text{tr}(\dot{\varepsilon}_{vp}) dt \quad (10)$$

where  $t$  is time,  $t_{cr}$  is the time at which coherent solid fraction is reached and damage begins to accumulate,  $g_s$  is the solid volume fraction,  $\text{tr}(\ )$  is the trace operation function for the volumetric contribution of the inelastic strains, and  $\dot{\varepsilon}_{vp}$  is the viscoplastic strain rate tensor. For the present study,  $t_{cr}$  was chosen as the time when the solid fraction reaches 0.5.

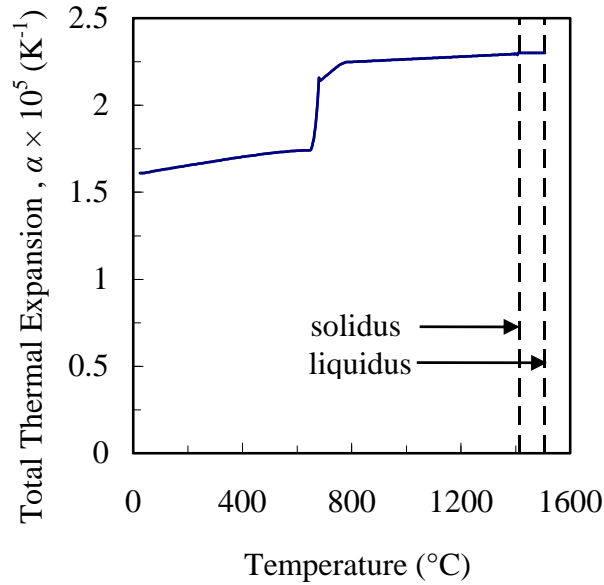


Figure 12. Coefficient of total thermal expansion was derived from the density of the Strained 1 experiment, as shown in Fig 11(a).

## 5. Mechanical Properties

The elastic properties were taken directly from the literature. Because experimental observations of increased Poisson's ratio with temperature may be due to increasing amounts of creep during the test<sup>8</sup>, a constant value of 0.3 was used for Poisson's ratio. The temperature-dependent Young's modulus, taken from Li and Thomas<sup>9</sup>, is shown in Fig. 16.

The viscoplastic properties were estimated using experimental data found in the literature. Wray<sup>10</sup> performed tensile tests on steel with a range of carbon contents and at varying strain rates from 850 °C to 1200 °C. Suzuki *et al.*<sup>11</sup> performed creep tests on steel from 1200 °C to 1400 °C.

The unknown viscoplastic parameters of equation (9) are  $\sigma_0$ ,  $n$ ,  $m$ ,  $\varepsilon_0$ , and  $\dot{\varepsilon}_0$ . The reference strain rate,  $\dot{\varepsilon}_0$ , is governed by the Arrhenius equation, i.e.,

$$\dot{\varepsilon}_0 = A \exp(-Q/RT) \quad (11)$$

where  $A$  is the Arrhenius prefactor,  $Q$  is the activation energy, and  $R$  is the universal gas constant. Using  $\varepsilon_0 = \sigma_0 n / E$ , five unknown parameters remain in equation (9) ( $\sigma_0$ ,  $n$ ,  $m$ ,  $A$ ,  $Q$ ). Three parameters ( $\sigma_0$ ,  $n$ , and  $m$ ) were assumed to be linear functions of temperature.  $A$  is carbon content-dependent<sup>12</sup> and was assumed to be a quadratic function, and  $Q$  is a temperature-independent constant. The parameters were estimated using a Levenberg-Marquardt least-squares minimization between the predicted and experimental stress. Estimated values are shown in Table 4, where  $T$  is in °C. The viscoplastic parameters ( $\sigma_0$ ,  $n$ , and  $m$ ) were linearly extrapolated up to the liquidus temperature and down to the solid-state transformation. As shown in Fig. 10, the mechanical strain below the solid-state transformation is negligible, and the total strain is the thermal strain. To ensure the model does not predict viscoplastic strain below the solid-state transformation, the following assumptions were made: (1) The initial yield stress,  $\sigma_0$ , was estimated from the literature<sup>13,14</sup> as a very high value, (2) The rate hardening exponent,  $n$ , was assumed to remain constant, and (3) The strain rate sensitivity exponent,  $m$ , decreased sharply to zero. Plots of the strain hardening and strain rate sensitivity exponents, initial yield stress, and reference strain and strain rates are shown in Figs. 17, 18, and 19, respectively.

The accuracy of a model can be measured by how well it fits the data from which its parameters were estimated. Fig. 20 shows a comparison of fitted model with the experimental

data, with the Root Mean Square errors (RMS) listed next to each curve. While the fit seems to be reasonable, there are some differences between the measured and predicted stresses, particularly at low strain rates. Recall from Fig. 10 that the mechanical strain rates of the strained bar experiment are on the order of  $10^{-5}$  1/s, which are similar to the lower strain rates in Fig. 20. The parameters were estimated over a wide range of strains, strain rates, and carbon constants. If measured and predicted displacements do not agree, the model may need to be re-fit to data that is representative of the current study. In total, 624 data points were used to estimate the parameters. The total RMS error was 0.898 MPa. A physical interpretation of this error is there is 95% confidence that predicted stress is approximately within  $\pm 2$  times the RMS value.

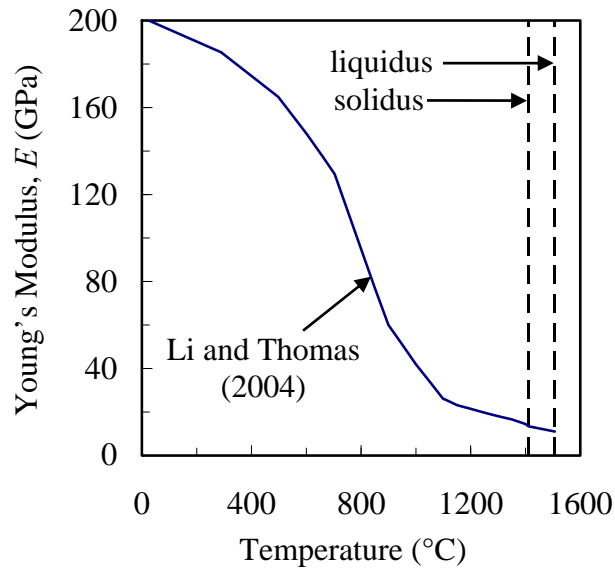


Figure 13. Young's Modulus.

## 6. Displacement Simulations

Simulations were performed in ABAQUS with a user-defined UMAT subroutine. The mechanical properties were input into the subroutine along with the solid phase fraction and the total thermal expansion. Thermal fields at approximately 200 time steps from the thermal simulations were transferred from the MAGMAsoft mesh to the ABAQUS mesh. To save computational costs, the metal in the pouring cup was not included in the simulations.



Table 4. Parameters for the viscoplastic equation. Parameters were estimated from the experimental data of Wray<sup>10</sup> and Suzuki *et al.*<sup>11</sup> Temperatures have units of °C and %C is the carbon content of the steel.

Parameter	Estimated Value
$\sigma_0$	$0.4634 - 4.60 \times 10^{-5} T$ [MPa]
$n$	$0.2436 - 5.98 \times 10^{-5} T$
$m$	$0.0615 + 8.80 \times 10^{-5} T$
$A$	$24869 + 124550(\%C) + 12400(\%C)^2$ [1/s]
$Q$	353 [kJ/mol]

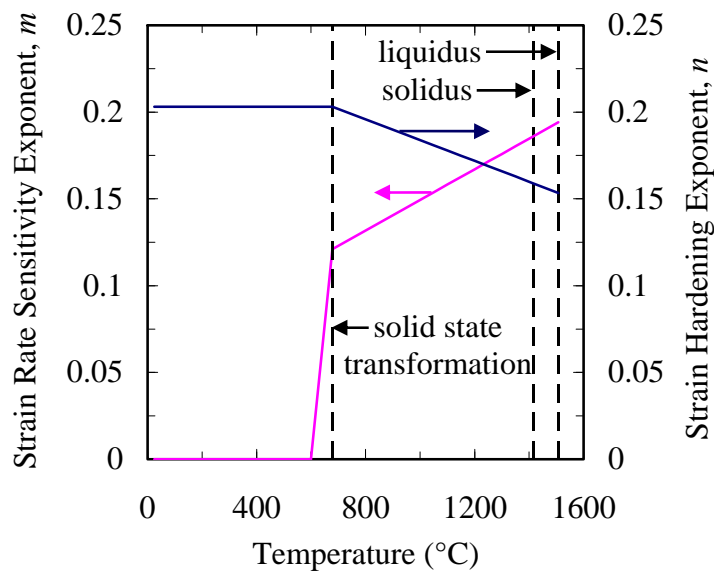


Figure 14. Strain rate sensitivity and strain hardening exponents. The exponents were estimated from the experimental data of Wray<sup>10</sup> and Suzuki *et al.*<sup>11</sup> from 850 °C to 1400 °C and extrapolated up to the liquidus temperature and down to the solid-state transformation. Below the solid-state transformation, the strain rate sensitivity exponent was assumed to decrease steeply to zero and the strain hardening exponent was assumed a constant value.

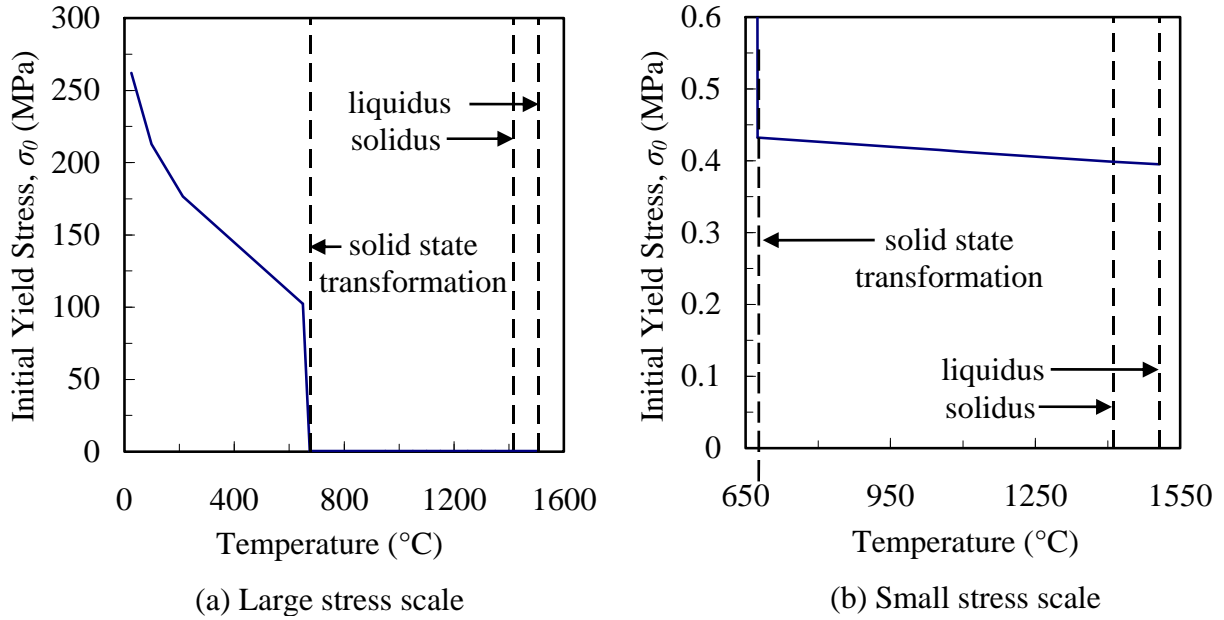


Figure 15. Initial yield stress. The initial yield stress was estimated from the experimental data of Wray<sup>10</sup> and Suzuki *et al.*<sup>11</sup> from 850  $^{\circ}\text{C}$  to 1400  $^{\circ}\text{C}$  and extrapolated up to the liquidus temperature and down to the solid-state transformation. Below the solid-state transformation, the initial yield stress was estimated from the literature<sup>13,14</sup>.

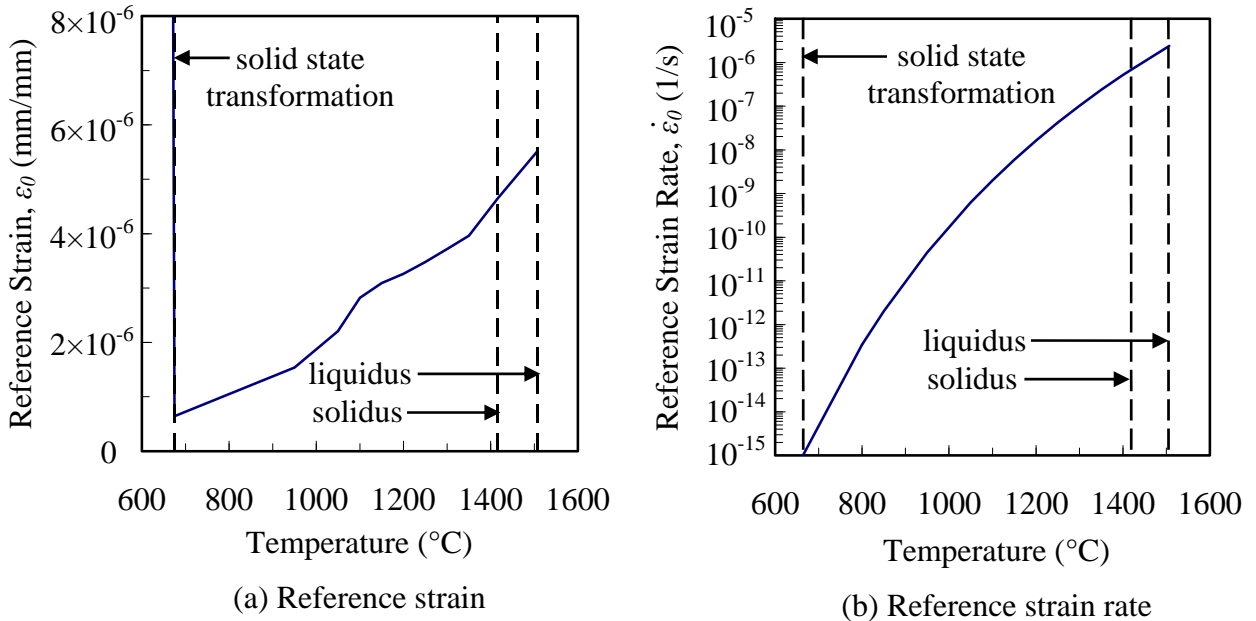


Figure 16. Reference strain and strain rate. The reference strain was calculated by  $\epsilon_0 = \sigma_0 \eta / E$ , and the reference strain rate was assumed to be governed by the Arrhenius equation, i.e.,  $\dot{\epsilon}_0 = A \exp(-Q/RT)$ . Unknown parameters were estimated from the experimental data of Wray<sup>10</sup> and Suzuki *et al.*<sup>11</sup>

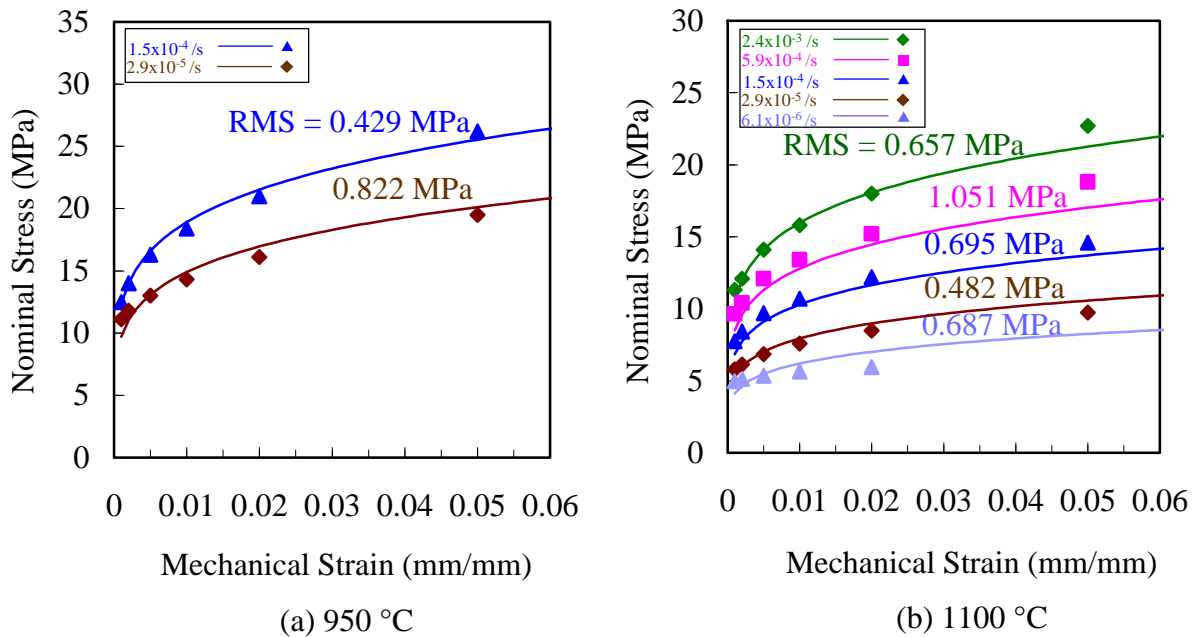


Figure 17. The predicted stresses of the model are compared to the experimental data from which its parameters were estimated. The plots show comparisons at different strain rates and a carbon content of 0.29%.

### 6.1 Unrestrained Bar

Displacement results for the unrestrained bar are shown in Fig. 21. Very good agreement is seen between measured and predicted displacements. Slight differences are seen immediately after the casting is poured and again near the solid-state transformation. Recall that there was uncertainty in the thermal simulations at temperatures above the solidus. This was a result of pouring the casting with a low superheat and not measuring the liquidus temperature due to the lag of the thermocouples. Additionally, the measured and predicted temperatures at the solid-state transformation could not be matched perfectly. These are likely the reasons for the mismatch between measured and simulated data. It can be assumed that the elastic and viscoplastic strains are negligible in the unrestrained bar, and the total strain in the bar is the thermal strain. Since the total thermal strain is derived from the changes in density as the material cools, the temperature-dependent density values that were predicted by IDS are seen to be very accurate.

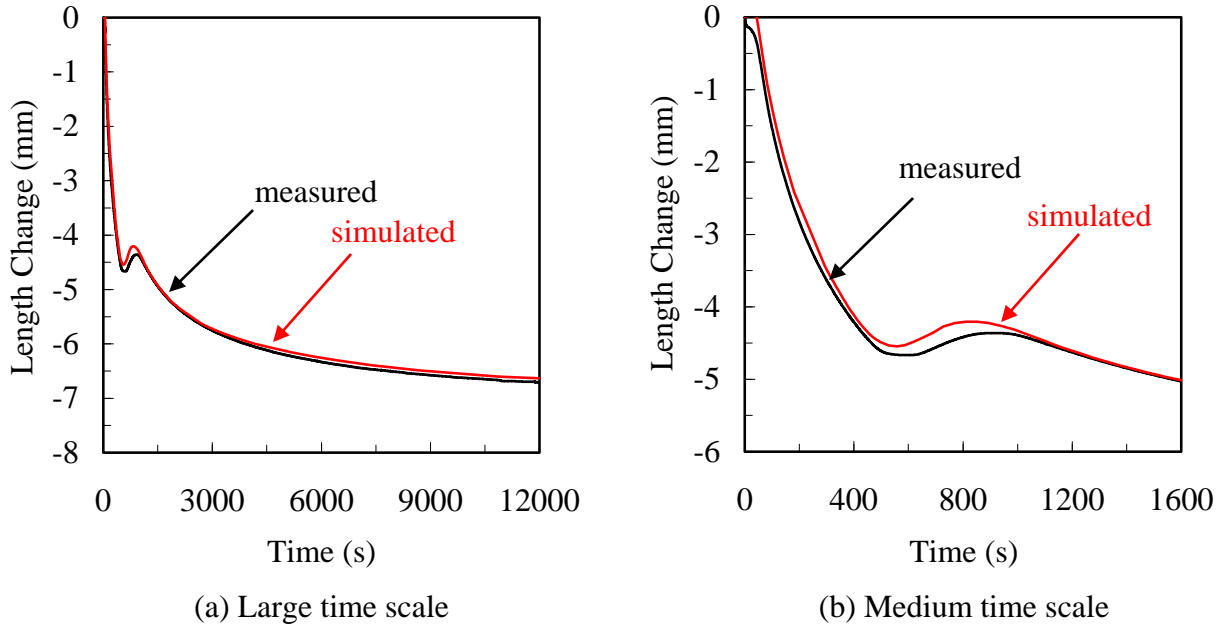


Figure 18. Displacement simulations of unrestrained bar.

## 6.2 Strained Bar

Displacement simulations of the strained bar are shown in Fig. 22. The simulations were performed using the non-turnbuckle force measurements as a boundary condition. The simulation shows good agreement until the midpoint of the straining region (shown in Fig. 22(a)). The simulated displacement is more sensitive to the applied forces than the measured displacement. Changes in the simulated displacement are abrupt, whereas the changes in the measured data are more gradual. After initially diverging from the measured curve during the induced straining period, the gap between the measured and simulated curves stabilizes and becomes constant from the solid-state transformation to room temperature. An adjusted simulation was also performed by adjusting the initial yield stress to a lower value, as shown in Fig. 23. This adjustment results in a significant difference between the curves initially but very good agreement after approximately 200 seconds.

Figs. 24 and 25 show the total equivalent plastic strain and von Mises stresses of the restrained bar after it has cooled to room temperature, respectively. Very little plastic strain occurs in the sprue. As expected, the majority of the plastic strain occurs near the hotspot in the casting and then decreases with increasing axial distance from the center of the bar. This is because the strength in the bar was the weakest near the hotspot during the induced straining

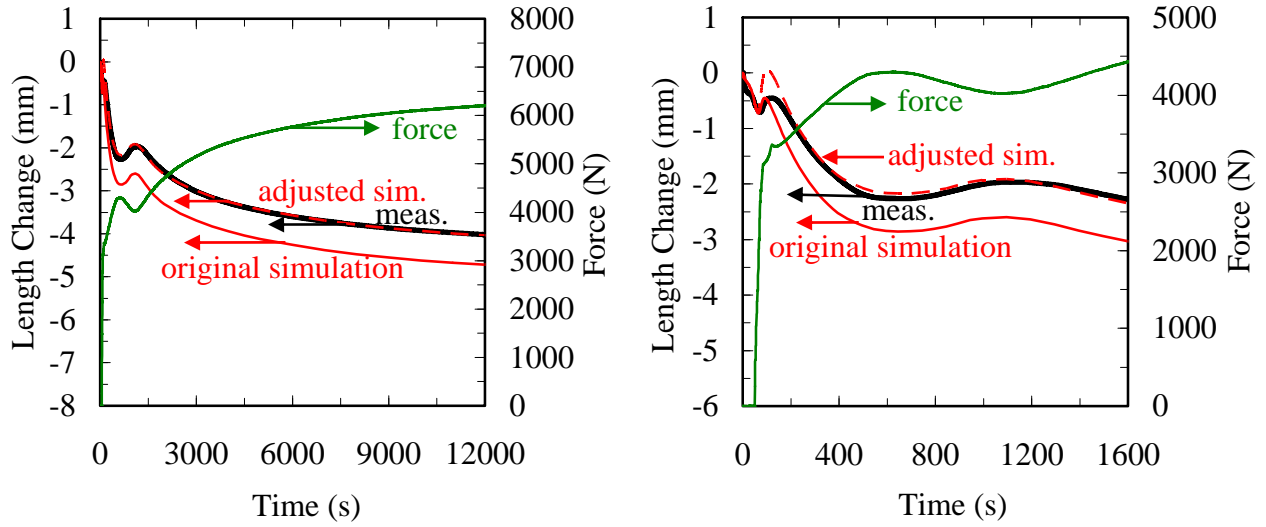
period. High magnitudes of plastic strains and stresses are shown in the hotspot near the sprue and around the ends of the restraining bolts, but these are due to the compressive forces that have built up during the cooling of the casting. The stresses in the majority of the bar are tensile and due to the forces transmitted through the restraining bolts. Finally, Fig. 26 shows minimal predicted damage in the restrained bar, with a maximum damage of approximately 0.4%.

## **7. Conclusion and Future Work**

Deformation in a steel casting was predicted using a viscoplastic deformation and stress model that considers damage. *In situ* casting experiments were performed to acquire thermal, force and displacement data. The thermal and force data were used to impose boundary conditions, and the predicted displacement was compared to the measured displacement for validation. Estimated parameters for the viscoplastic model were obtained from stress-strain data found in the literature. Predicted displacement in the unrestrained bar showed very good agreement with the measured displacement. The results of the strained bar simulation show promise, but more work is needed to achieve better agreement. The discrepancy between the measured forces of the load bolts is also a concern, and could be a cause of the measured and predicted differences. Future work will also include modeling the interaction between the mold and the casting.

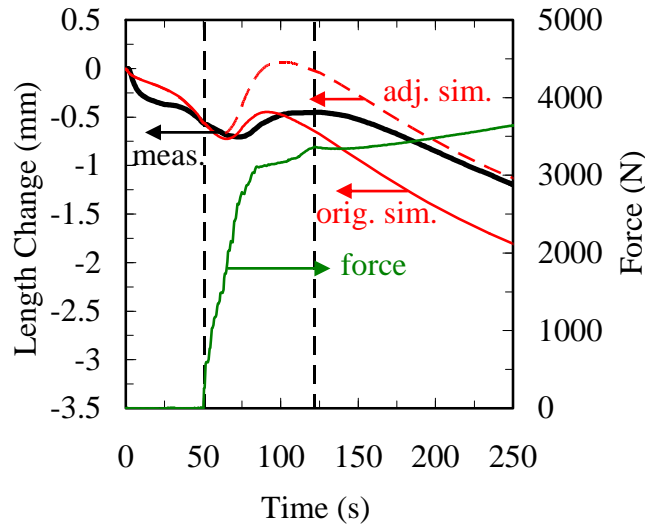
## **Acknowledgements**

Special thanks to Jerry Thiel, Brodie Biersner, and the other students from the Metal Casting Center at the University of Northern Iowa for their assistance with the casting experiments.



(a) Large time scale

(b) Medium time scale



(c) Small time scale

Figure 19. Displacement simulations of strained bar using a force boundary condition. The original simulation was run using the parameters estimated from the experimental data of Wray<sup>10</sup> and Suzuki *et al.*<sup>11</sup>. For the adjusted simulation, the value of the initial yield stress was lowered to match the final simulated and measured length changes of the bar. The difference between the initial and adjusted initial yield stresses is shown in Fig. 23.

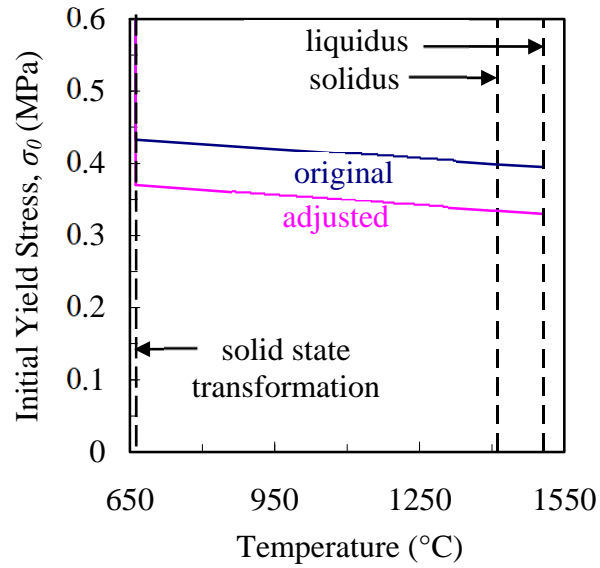


Figure 20. The original yield strength values were estimated from Wray<sup>10</sup> and Suzuki *et al.*<sup>11</sup>. The adjusted yield strength values were adjusted to obtain agreement between predicted and measured length changes of the bar.

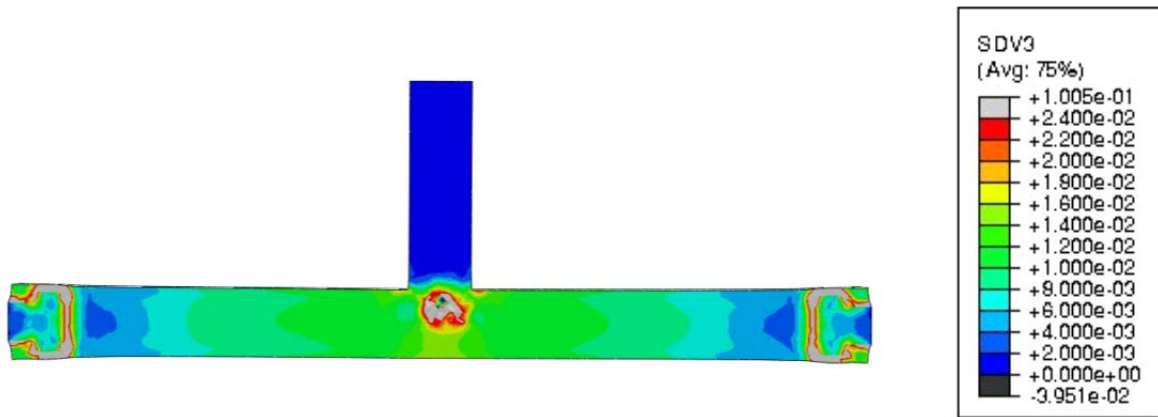


Figure 21. Equivalent plastic strain in strained bar at the end of the simulation (deformation scale factor of 6).

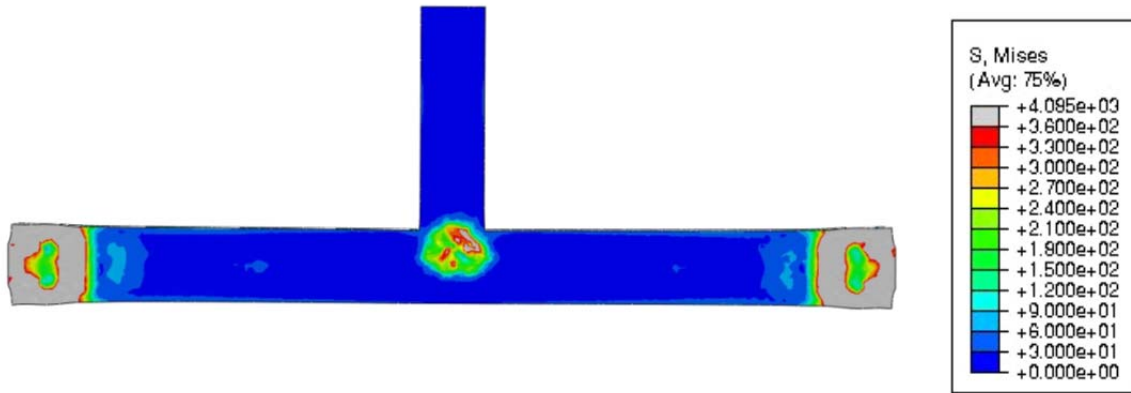


Figure 22. Von Mises stress in strained bar at the end of the simulation (deformation scale factor of 6).

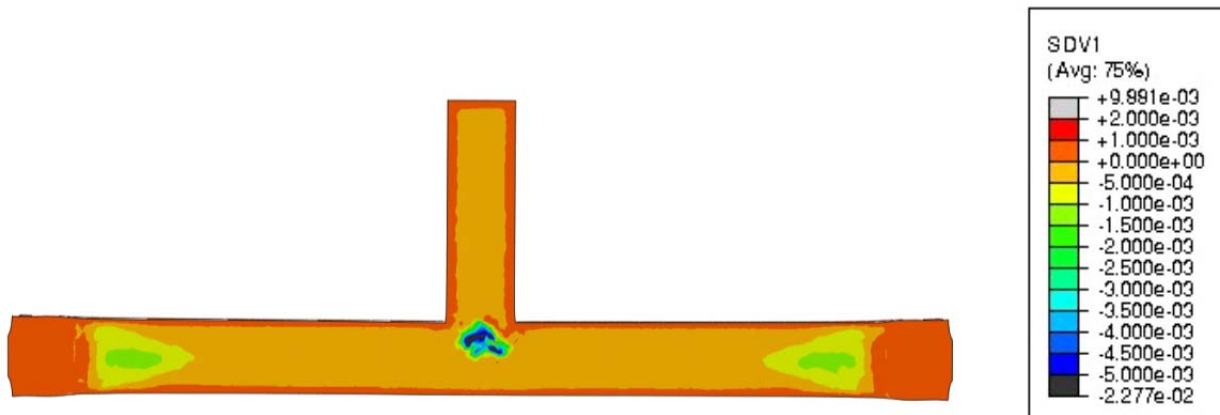


Figure 23. Integrated damage in strained bar at the end of the simulation (deformation scale factor of 6).



## References

1. *MAGMASoft*, MAGMA GmbH, Kackerstrasse 11, 52072 Aachen, Germany.
2. *Abaqus/Standard*, Abaqus, Inc., Providence, RI, 2006.
3. Bichler, L., Elsayed, A., Lee, K., and Ravindran, C., "Influence of Mold and Pouring Temperatures on Hot Tearing Susceptibility of AZ91D Magnesium Alloy", *International Journal of Metalcasting*, vol. 2, no. 1, pp 45-56, 2008.
4. Monroe, C., and Beckermann, C., "Development of a Hot Tear Indicator for Steel Castings", *Materials Science and Engineering A*, vol. 413-414, pp 30-36, 2005.
5. Rowan, M., Thomas, B.G., Pierer, R., Bernhard, C., "Measuring Mechanical Behavior of Steel During Solidification: Modeling the SSCC Test", *Metallurgical and Materials Transactions B*, vol. 42, no. 4, pp 837-851, August 2011.
6. J. Miettinen, "Calculation of Solidification-related Thermophysical Properties for Steels", *Metallurgical and Materials Transactions B*, vol. 28, no. 2, pp 281-297, April 1997.
7. Marin, E.B., and McDowell, D.L., "A Semi-implicit Integration Scheme for Rate-dependent and Rate-independent Plasticity", *Computers and Structures*, vol. 63, no.3, pp 30-36, 2005.
8. Brian G. Thomas, "Issues in Thermal-mechanical Modeling of Casting Processes", *ISIJ International*, vol. 35, no. 6, pp 737-743, 1995.
9. Chunsheng Li and Brian G. Thomas, "Thermomechanical Finite-element Model of Shell Behavior in Continuous Casting of Steel", *Metallurgical and Materials Transactions B*, vol. 35B, pp 1151-1172, December 2004.
10. Peter J. Wray, "Effect of Carbon Content on the Plastic Flow of Plain Carbon Steels at Elevated Temperatures", *Metallurgical Transactions A*, vol. 13A, no. 1, pp 125-134, 1982.
11. T. Suzuki, K.H. Tacke, K. Wunnenberg, and K. Schwerdtfeger, "Creep Properties of Steel at Continuous Casting Temperatures", *Ironmaking and Steelmaking*, vol. 15, no. 2, pp 90-100, 1988.
12. Peter J. Wray, *Modeling of Casting and Welding Processes*, pp 245-257, AIME Conference Proceedings, Rindge, NH, 1980.
13. *Structural Alloys Handbook*, vols. 1 and 2, D.J. Maykuth, Ed. , Mechanical Properties Data Center, Batelle Columbus Laboratories, 1980.
14. Monroe, C., Ph.D. thesis, University of Iowa, Iowa City, 2008.